

Higher winding number in a nonunitary photonic quantum walkLei Xiao,^{1,2} Xingze Qiu,^{3,4} Kunkun Wang,^{1,2} Zhihao Bian,^{1,2} Xiang Zhan,^{1,2} Hideaki Obuse,⁵ Barry C. Sanders,^{6,7,8} Wei Yi,^{3,4,*} and Peng Xue^{1,2,9,†}¹*Beijing Computational Science Research Center, Beijing 100084, China*²*Department of Physics, Southeast University, Nanjing 211189, China*³*Key Laboratory of Quantum Information, University of Science and Technology of China, CAS, Hefei 230026, China*⁴*Synergetic Innovation Center in Quantum Information and Quantum Physics, University of Science and Technology of China, CAS, Hefei 230026, China*⁵*Department of Applied Physics, Hokkaido University, Sapporo 060-8628, Japan*⁶*Hefei National Laboratory for Physical Sciences at Microscale, University of Science and Technology of China, CAS, Hefei 230026, China*⁷*Institute for Quantum Science and Technology, University of Calgary, Alberta, Canada T2N 1N4*⁸*Program in Quantum Information Science, Canadian Institute for Advanced Research, Toronto, Ontario, Canada M5G 1M1*⁹*State Key Laboratory of Precision Spectroscopy, East China Normal University, Shanghai 200062, China*

(Received 12 February 2018; published 28 December 2018)

Topological matter exhibits exotic properties yet phases characterized by large topological invariants are difficult to implement, despite rapid experimental progress. A promising route toward higher topological invariants is via engineered Floquet systems, particularly in photonics, where flexible control holds the potential of extending the study of conventional topological matter to novel regimes. Here we implement a one-dimensional photonic quantum walk to explore large winding numbers. By introducing partial measurements and hence loss into the system, we detect winding numbers of three and four in multistep nonunitary quantum walks, which agree well with theoretical predictions. Moreover, by probing statistical moments of the walker, we identify locations of topological phase transitions in the system and reveal the breaking of pseudounitary near topological phase boundaries. As the winding numbers are associated with nonunitary time evolution, our investigation enriches understanding of topological phenomena in nonunitary settings.

DOI: [10.1103/PhysRevA.98.063847](https://doi.org/10.1103/PhysRevA.98.063847)**I. INTRODUCTION**

Topological phases are typically characterized by integer-valued topological invariants, associated with the emergence of robust edge states through the so-called bulk-boundary correspondence [1–4]. Recent experiments reveal and characterize topological edge states and bulk topological invariants in settings ranging from condensed matter [1,5,6] to synthetic systems [7–30]. However, the experimentally detected topological invariants are typically small and limited to two [15,21–31]. Whereas bands with Chern numbers greater than two have been engineered in photonic materials in two dimensions [10], direct detection of Chern numbers greater than two has yet to be achieved. In one dimension, while topological phases with large winding numbers have been theoretically studied, e.g., in quantum transport [32] or in quantum-walk dynamics [33,34], experimental realization is still lacking. Besides fundamental theoretical interest in generating and studying topological phases characterized by larger topological invariants, these phases support more topological edge states at appropriately engineered boundaries, which are a valuable resource for applications in quantum information and in topological photonics [8,13].

A promising platform for detection of large bulk topological invariants is synthetic Floquet topological systems, where winding numbers of two have been probed through losses in either continuous-time non-Hermitian dynamics of light propagating in optical waveguide array [30] or nonunitary discrete-time photonic quantum walks (QWs) [26]. Interestingly, detected topological invariants in these lossy systems can be associated with underlying non-Hermitian [30,32] or nonunitary Floquet dynamics [26], respectively. These studies reveal topological properties in non-Hermitian or nonunitary settings, and establish a new paradigm of topology that is difficult to access in conventional condensed-matter systems [32,35].

In this work, we report experimental detection of large winding numbers of three and four in photonic nonunitary QWs. By periodical partial measurements on polarization of the photonic walker, we realize multistep nonunitary QWs in one dimension supporting Floquet topological phases (FTPs). As for two-step nonunitary QWs, partial measurement introduces loss to the quantum-walk dynamics and provides a natural detection channel for FTP winding number [26,36]. Whereas FTPs in two-step nonunitary QWs are directly related to those in a lossy Su-Schrieffer-Heeger (SSH) model [26,35], the multistep nonunitary QWs here are analogous to adding longer-range hopping terms in the lossy SSH model, which gives rise to higher winding numbers. We directly detect winding numbers of three and four through average

*wyiz@ustc.edu.cn

†gnep.eux@gmail.com

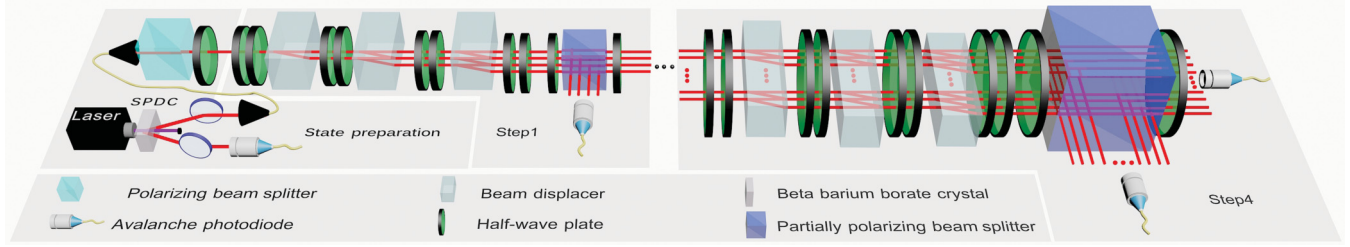


FIG. 1. We show a three-step nonunitary QW up to four time steps as an example. The photon pair is created via spontaneous parametric down conversion. One photon serves as a trigger. The other photon is projected into the polarization state $|+\rangle$ with a polarizing beam splitter (PBS) and a half-wave plate (HWP, at 22.5°) and then proceeds through the quantum-walk interferometric network. The polarization rotation R and the polarization-dependent shift S are realized by two HWPs with certain setting angles depending on the coin parameters (θ_1, θ_2) and a beam displacer (BD) whose optical axis is cut so that the photons in $|V\rangle$ are directly transmitted and those in $|H\rangle$ undergo a lateral displacement into a neighboring spatial mode, respectively. The partial measurement via loss M_e is implemented by a sandwich-type HWP (at 22.5°) -PPBS-HWP (at 22.5°) setup (here, PPBS is the abbreviation for a partially polarizing beam splitter). For horizontally and vertically polarized photons, the transmissivity of the PPBS is $(T_H, T_V) = (1, 1 - p)$. Finally, the photons are detected by avalanche photodiodes (APDs), in coincidence with the trigger photons. Photon counts give measured probabilities after correcting for relative efficiencies of the different APDs.

displacements, and demonstrate topological phase transitions between FTPs with different topological invariants by probing statistical moments of the walker. We also directly demonstrate the breaking of pseudounitary near topological phase boundaries. Our experimental detection of large winding numbers in nonunitary FTPs offers the exciting prospect of exploring topological phases characterized by large topological invariants in nonunitary or non-Hermitian settings, which will create further opportunities in engineering unconventional topological phenomena using photonics.

II. MULTISTEP NONUNITARY QWs

We introduce the photonic setup for multistep nonunitary QWs, where the walker is shifted more than twice at each time step. We focus on three- and four-step nonunitary QWs in this work. As illustrated in Fig. 1, the three-step QW is on a one-dimensional homogeneous lattice L ($L \in \mathbb{Z}$), and the dynamics is governed by the Floquet operator [37]

$$\tilde{U}'_3 := MU'_3 = MR\left(\frac{\theta_1}{2}\right)SR(\theta_2)SR(\theta_2)SR\left(\frac{\theta_1}{2}\right). \quad (1)$$

Here, the coin operator $R(\theta)$ rotates single-photon polarization by θ about the y axis, where coin states are horizontally polarized ($|H\rangle$) and vertically polarized ($|V\rangle$). The polarization-dependent shift operator S moves the walker with coin state $|H\rangle$ ($|V\rangle$) to the left (right) by one lattice site. Nonunitary dynamics is enforced by the loss operator

$$M = \mathbb{1}_w \otimes (|+\rangle\langle+| + \sqrt{1-p}|-\rangle\langle-|), \quad 0 < p \leq 1, \quad (2)$$

where $|\pm\rangle = (|H\rangle \pm |V\rangle)/\sqrt{2}$, and $\mathbb{1}_w = \sum_L |x\rangle\langle x|$ with x denoting the position of the walker. The loss operator is equivalent to performing a partial measurement $M_e = \mathbb{1}_w \otimes \sqrt{p}|-\rangle\langle-|$ in the basis $\{|+\rangle, |-\rangle\}$ at each time step, with p the probability of a successful measurement.

Whereas R and S are implemented by using appropriate wave plates and beam displacers (BDs) [38–45], the partial measurement operator M_e is realized by a sandwich-type setup involving two half-wave plates (HWPs) and a partially polarizing beam splitter (PPBS) [26]. At each measurement

step in the quantum-walk dynamics, photons in the state $|-\rangle$ are reflected by the PPBS with probability p . Photons are then detected by single-photon avalanche photodiodes (APDs) and lost from the quantum-walk dynamics.

Topological properties in the experimental three-step nonunitary QW are introduced via the effective non-Hermitian Hamiltonian $H_{\text{eff}}^{(3)}$ defined through $\tilde{U}'_3 = \exp[-iH_{\text{eff}}^{(3)}]$ [36,37]. For the homogeneous single-photon QW considered here, $H_{\text{eff}}^{(3)}(k) = E_k \mathbf{n} \cdot \boldsymbol{\sigma}$ in momentum k space, with $\boldsymbol{\sigma}$ the Pauli vector, E_k the quasienergy spectrum, and \mathbf{n} the direction of the spinor eigenvector for each momentum $-\pi < k \leq \pi$. Similar to the case of the two-step nonunitary QW [26], the winding number of the three-step QW, which serves as a topological invariant of the system, is the number of times the real component of \mathbf{n} winds around the x axis as k varies through the first Brillouin zone.

For a given FTP with chiral symmetry, two distinct winding numbers (ν' , ν'') exist for Floquet operators fitted in different time frames [33]. Whereas the corresponding winding number for \tilde{U}'_3 is ν' , ν'' is similarly defined through the winding of the spinor eigenvector of the non-Hermitian Hamiltonian $H_{\text{eff}}^{(3)}$, where $\tilde{U}'_3 = \exp[-iH_{\text{eff}}^{(3)}]$ and

$$\tilde{U}'_3 := MS_{\text{up}}R(\theta_2)SR(\theta_1)SR(\theta_2)S_{\text{down}}. \quad (3)$$

Here, $S_{\text{up}} = \sum_x (|x+1\rangle\langle x| \otimes |V\rangle\langle V| + |x\rangle\langle x| \otimes |H\rangle\langle H|)$ and $S_{\text{down}} = \sum_x (|x\rangle\langle x| \otimes |V\rangle\langle V| + |x-1\rangle\langle x| \otimes |H\rangle\langle H|)$. Depending on the coin parameters, the absolute value of the winding numbers can take large integer values up to three, as we show in the phase diagram in Fig. 2(a).

Similar to three-step QWs, we define four-step nonunitary QWs from constructing the evolution operators

$$\tilde{U}'_4 := MR\left[\frac{\theta_{1(2)}}{2}\right]SR(0)SR[\theta_{2(1)}]SR(0)SR\left[\frac{\theta_{1(2)}}{2}\right]. \quad (4)$$

By analyzing the effective non-Hermitian Hamiltonians $H_{\text{eff}}^{(4)}$ and $H_{\text{eff}}^{(4)}$ respectively associated with the Floquet operators \tilde{U}'_4 and U''_4 , it is straightforward to demonstrate that FTPs exist for four-step QWs, which are characterized by integer-valued winding numbers as large as four. Importantly, both the

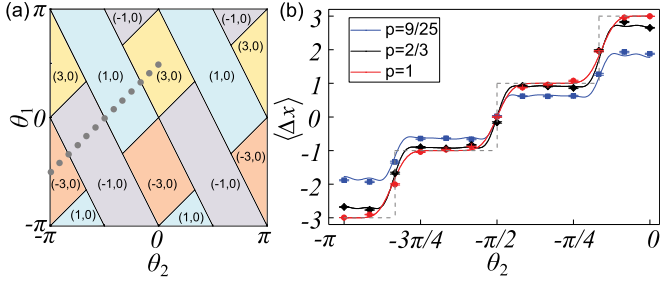


FIG. 2. (a) Phase diagram for three-step nonunitary QWs characterized by the topological invariants (ν', ν'') as functions of the coin parameters (θ_1, θ_2) . (ν', ν'') are calculated from the Floquet operators \tilde{U}'_3 and \tilde{U}''_3 , respectively. (b) Measured average displacements of three-step nonunitary QWs corresponding to \tilde{U}'_3 with different loss parameters $p = 1, 2/3, 9/25$. Coin parameters vary along the line $\theta_1 = \theta_2 + \pi/2$, as indicated by dots in Fig. 2(a). The dashed curve indicates expected results of infinite-step QWs. The solid curve indicates numerical simulations for QWs with four time steps and the experimental results are presented by dots. Experimental errors are due to photon-counting statistics.

three- and four-step QWs defined in Eqs. (1), (3), and (4) have chiral symmetry in the unitary limit ($p = 0$), with the chiral symmetry operator given by $\Gamma = \sigma_x$ as $\Gamma U \Gamma = U^{-1}$ (see the Appendixes), where U designates the Floquet operator of the corresponding QW. Consistent with previous studies [32], we find that topological properties of the nonunitary quantum-walk dynamics derive from those in the unitary limit, which are in turn protected by chiral symmetry. Hence chiral symmetry in the unitary limit is crucial for the perseverance of the FTPs in the nonunitary case ($p > 0$). Such a requirement restrains the available forms of nonunitary Floquet operators, of which Eqs. (1), (3), and (4) are the most straightforward examples (see the Appendixes).

III. WINDING NUMBERS AND THE BULK-BOUNDARY CORRESPONDENCE

We define winding numbers for multistep nonunitary QWs and discuss their relation with the topological edge states.

We write the Floquet operator

$$\tilde{U}'_3 = n_0 \sigma_0 - i n_1 \sigma_x - i n_2 \sigma_y - i n_3 \sigma_z \quad (5)$$

in momentum space. We then define a new vector $\mathbf{h} := \frac{1}{\|\text{Re}(\mathbf{n})\|} \text{Re}(\mathbf{n})$, with $\mathbf{n} = (\mathbf{n}_1, \mathbf{n}_2, \mathbf{n}_3)^T$. As $h_1 = \frac{1}{\|\text{Re}(\mathbf{n})\|} \text{Re}(n_1) = 0$ for all k , the topological invariant for the nonunitary QW is

$$\nu' := -\frac{1}{2\pi} \oint dk \left(\mathbf{h} \times \frac{\partial \mathbf{h}}{\partial k} \right)_1 \quad (6)$$

Following a similar procedure, we define the winding number ν'' for the Floquet operator \tilde{U}''_3 .

In the unitary limit with $p = 0$, n_1 becomes zero and the Floquet operators \tilde{U}'_3 and \tilde{U}''_3 manifestly satisfy chiral symmetry, with the chiral symmetry operator being $\Gamma = \sigma_x$. We define [33]

$$(\nu_0, \nu_\pi) := \left(\frac{\nu' + \nu''}{2}, \frac{\nu' - \nu''}{2} \right), \quad (7)$$

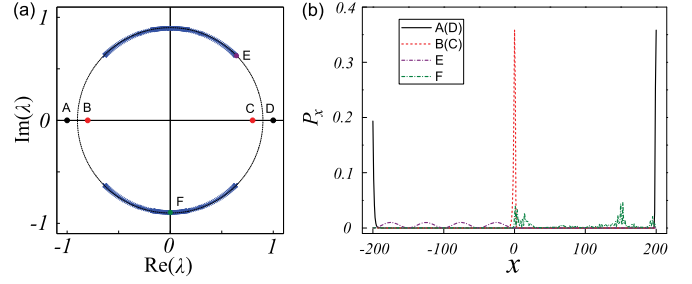


FIG. 3. (a) Eigenspectrum of λ on the complex plane. The blue dots correspond to bulk states and the red (black) dots correspond to topological edge states located near $x = 0$ and $x = \pm 200$, respectively. There are altogether four edge states in the spectrum. (b) The spatial probability distribution of the edge states corresponding to the red and black dots in (a).

which are directly related to edge states at the boundaries with quasienergies zero and π , respectively. Specifically, the number of edge states with quasienergy zero (π) should be equal to the difference in the winding numbers ν_0 (ν_π) on either side of the boundary. For the nonunitary QW ($p > 0$), the Floquet operators no longer possess chiral symmetry, and the bulk-boundary correspondence between the bulk winding numbers and the topological edge states needs to be confirmed. We have checked numerically that the topological invariants ν_0 and ν_π are related to localized topological edge states with the real parts of quasienergies at zero and π , respectively.

We consider an inhomogeneous three-step QW on a lattice with 401 sites and with a periodic boundary condition. The nonunitary QW is governed by the Floquet operator \tilde{U}'_3 with $p = 9/25$. We introduce two boundaries near $x = 0$ and $x = \pm 200$, with $(\theta_1^L, \theta_2^L) = (\pi/4, -\pi/4)$ for $-200 \leq x < 0$ and $(\theta_1^R, \theta_2^R) = (\pi/2, 0)$ for $0 \leq x \leq 200$. According to the phase diagram in Fig. 2(a), the winding numbers for $-200 \leq x < 0$ are $(\nu', \nu'') = (1, 0)$ and those for $0 \leq x \leq 200$ are $(\nu', \nu'') = (3, 0)$. Therefore, we have $(\nu_0^L, \nu_\pi^L) = (\frac{1}{2}, \frac{1}{2})$ for $-200 \leq x < 0$ and $(\nu_0^R, \nu_\pi^R) = (\frac{3}{2}, \frac{3}{2})$ for $0 \leq x \leq 200$.

At both boundaries, the differences between the winding numbers are $\delta\nu_0 = |\nu_0^L - \nu_0^R| = 1$ and $\delta\nu_\pi = |\nu_\pi^L - \nu_\pi^R| = 1$. This should correspond to a pair of topological edge states at each edge, with the real part of their quasienergies at zero and π , respectively. In the following, we confirm this expectation by numerically calculating the quasienergy spectrum.

We define the effective Hamiltonian $\tilde{U}'_3 = \exp(-i H_{\text{eff}})$. The quasienergy ϵ is defined as

$$\tilde{U}'_3 |\psi_\lambda\rangle = \lambda |\psi_\lambda\rangle, \quad \lambda = e^{-i\epsilon}, \quad (8)$$

where $|\psi_\lambda\rangle$ is the eigenstate of \tilde{U}'_3 and H_{eff} . In Fig. 3(a), we plot the eigenspectrum of λ on the complex plane. Whereas the blue dots are the bulk states, the red (B and C) and the black (A and D) dots appearing on the real axis correspond to localized edge states at the two boundaries near $x = 0$ and $x = \pm 200$, respectively. Localization of the edges states is confirmed by plotting the probability distribution $P_x = \langle \psi_\lambda | x \rangle \langle x | \otimes \mathbb{1}_c | \psi_\lambda \rangle$ of the edge states (A, B, C, and D), as illustrated in Fig. 3(b).

For comparison, we have shown typical spatial distributions of the bulk states (E and F), which are indeed extended in

space. Importantly, near $x = 0$, there exist two localized edge states with identical spatial distributions, which correspond to the red dots (B and C) in Fig. 3(a). The real parts of the corresponding quasienergy ϵ are given by π (B) and zero (C), respectively. The case at the boundary near $x = \pm 200$ is similar. For comparison, we have also shown typical spatial distributions of the bulk states (E and F), which are indeed extended in space. This confirms the bulk-boundary correspondence as discussed in the previous paragraph. We have checked that such a bulk-boundary correspondence works for other choices of coin parameters throughout the phase diagram in Fig. 2(a). For brevity, we use the three-step nonunitary QW as an example. The case with the four-step nonunitary QW is similar.

IV. DETECTING TOPOLOGICAL INVARIANTS FROM LOSSES

In two-step nonunitary QWs, topological invariants can be probed by monitoring losses [26,35,36]. As we experimentally demonstrate and explain, topological invariants of the multistep nonunitary QWs are determined from losses by measuring average displacement

$$\langle \Delta x \rangle = \sum_x \sum_{t'=1}^{\infty} x P_{\text{th}}(x, t'), \quad (9)$$

for the walker-coin system initialized in the state $|\psi_0\rangle = |x=0\rangle \otimes |+\rangle$. Here, the probability of the walker being detected at x during the t th time step is

$$P_{\text{th}}(x, t) = \langle \psi_{t-1} | U_3^\dagger M_e^\dagger(|x\rangle\langle x| \otimes \mathbb{1}_c) M_e U_3 | \psi_{t-1} \rangle, \quad (10)$$

where $|\psi_t\rangle = (\tilde{U}_3^t) |\psi_0\rangle$ and $\mathbb{1}_c$ is a 2×2 identity operator.

To experimentally probe the average displacement in the nonunitary QW with t steps in total, we perform coincidence measurements on the number of the reflected photons $N_R(x, t')$ ($t' = 1, \dots, t$) at each position successively up to t . We then construct the probability

$$P_{\text{exp}}(x, t) = \frac{N_R(x, t')}{\sum_{x'} [\sum_{t''=1}^t N_R(x', t'') + N_T(x', t)]}, \quad (11)$$

where $N_T(x, t)$ is the number of transmitted photons at the last step t . The average displacement is then

$$\langle \Delta x \rangle_{\text{exp}} = \sum_x \sum_{t'=1}^t x P_{\text{exp}}(x, t'). \quad (12)$$

To detect topological invariants, we realize three-step nonunitary QWs with three different loss parameters $p = 1, 2/3, 9/25$. The corresponding phase diagram is shown in Fig. 2(a), where the topological invariants (ν' , ν'') are functions of the coin parameters (θ_1, θ_2). Thirteen sets of coin parameters (θ_1, θ_2) are chosen along the line $\theta_1 = \theta_2 + \pi/2$, as indicated in Fig. 2(a). The topological invariant ν' assumes values $-3, -1, 1$ to 3 along the line, while ν'' is fixed at zero. The walker starts from $x = 0$ and the initial coin state is chosen to be $|+\rangle$.

Measured average displacements are shown in Fig. 2(b) for the Floquet operator \tilde{U}_3' (as ν'' is always zero, the average displacements for \tilde{U}_3'' are not shown). These results agree

well with the numerical simulations of three-step QWs up to four time steps and demonstrate plateaux close to the quantized values of ν' calculated for QWs with infinite time steps. We observe that with increasing loss parameter p , measured average displacements at a given time step converge faster to the quantized values. This result is consistent with the measurement results for two-step nonunitary QWs [26] and suggests that the quantum Zeno effect is weak in these systems [36]. For systems with a strong quantum Zeno effect, $|-\rangle$ becomes effectively unoccupied in the limit of $p = 1$, which results in a longer convergence time with increasing p . Meanwhile, regardless of the loss parameter, it takes much longer for the displacements to converge near topological phase transitions, where the topological invariants undergo abrupt changes.

We then implement four-step nonunitary QWs with various loss parameters $p = 1, 2/3, 9/25$. The corresponding phase diagram is shown in Fig. 4(a). As the coin parameters vary along the dotted line $\theta_1 = \theta_2 + \pi/2$ in the phase diagram, the topological invariants (ν', ν'') change from $(-4, 0)$, $(0, -4)$, $(4, 0)$, to $(0, 4)$. The measured average displacements for the operators \tilde{U}_4' and \tilde{U}_4'' up to three time steps are shown in Figs. 4(b) and 4(c), respectively, which agree well with the corresponding numerical simulations.

V. CONFIRMING THE TOPOLOGICAL PHASE TRANSITIONS

We confirm the topological phase boundaries, signaled by jumps of the measured topological invariants, by probing statistical moments [11]. Specifically, we define the second statistical moment of the walker after t steps as

$$m_2(t) := \frac{\sum_x x^2 \langle \psi_t | x \rangle \langle x | \otimes \mathbb{1}_c | \psi_t \rangle}{\sum_x \langle \psi_t | x \rangle \langle x | \otimes \mathbb{1}_c | \psi_t \rangle}. \quad (13)$$

Experimentally, the moment is evaluated from the spatial distribution of the transmitted photons at the last step t :

$$m_2^{\text{exp}}(t) = \sum_x x^2 \frac{N_T(x, t)}{\sum_{x'} N_T(x', t)}. \quad (14)$$

In a unitary quantum walk, the bulk gap closes at the topological phase boundaries, which leads to nonanalyticities of the statistical moments at critical points [11]. Anomalies in the second statistical moments also exist in nonunitary quantum walks, but in a different form. In Fig. 5, we plot the measured values for $m_2^{\text{exp}}(t)/t^2$ of multistep nonunitary QWs with two different loss parameters $p = 2/3, 9/25$. In (a),(c), coin parameters are scanned along the dotted lines in the phase diagrams. We find reasonable agreement between experimental results and numerical simulations. Importantly, $m_2^{\text{exp}}(t)/t^2$ features precipitous dips centered at the topological phase boundary. This is reflected in numerical simulations of long-time dynamics, as well as in the measured $m_2^{\text{exp}}(t)/t^2$ at short times under appropriate parameters [see Figs. 5(b) and 5(d)].

The dips in $m_2^{\text{exp}}(t)/t^2$ are closely related to a hidden pseudounitariness of the Floquet operators. A Floquet operator U is pseudounitary if it satisfies $U^{-1} = \eta U^\dagger \eta^{-1}$, where η is a Hermitian invertible linear operator [46]. Existence of

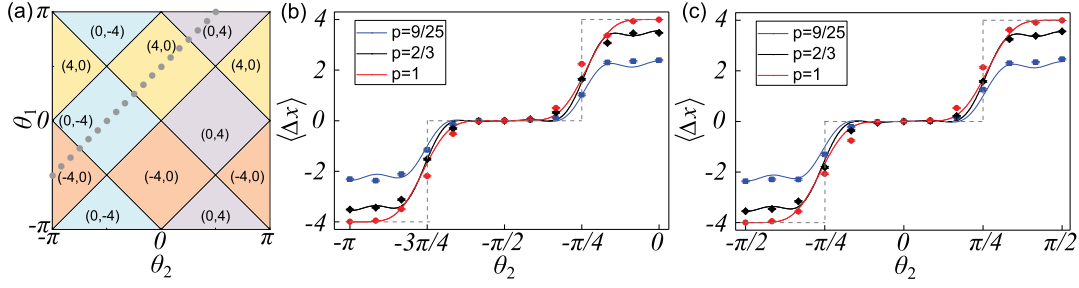


FIG. 4. (a) Phase diagram for four-step nonunitary QWs in terms of the topological invariants (v', v'') . (v', v'') are calculated from the Floquet operators \tilde{U}'_4 and \tilde{U}''_4 , respectively. Measured average displacements of four-step nonunitary QWs of \tilde{U}'_4 (b) and \tilde{U}''_4 (c) with different loss parameters $p = 1, 2/3, 9/25$. Coin parameters vary along the line $\theta_1 = \theta_2 + \pi/2$ as indicated by dots in Fig. 4(a). Experimental errors are due to photon-counting statistics.

the pseudounitariness guarantees the reality of the quasienergy spectra of the corresponding effective non-Hermitian Hamiltonian. In the case of broken pseudounitariness, however, the quasienergy spectra become complex, which subsequently influence the resulting dynamics. For the three- and four-step nonunitary QWs considered here, the Floquet operators can be mapped (see the Appendixes), by a statistical-moment-preserving scaling, to operators with pseudounitariness [46–48]. In the vicinity of topological phase boundaries (see the Appendixes), pseudounitariness is lost, which gives rise to imaginary-valued quasienergy spectra. Nonunitary QWs in these regions are therefore analogous to those with broken parity-time symmetry, where the long-time spatial distribution of the walker is Gaussian-like rather than ballistic [12,49,50]. This spreading property leads directly to a drop of the second moment in the nonpseudounitary regions.

Further, from long-time numerical simulations shown in Fig. 5, we identify nonanalytical peaks in $m_2^{\text{exp}}(t)/t^2$, located on both sides of a dip and at the boundary between regions with and without pseudounitariness. At these pseudounitariness

boundaries, the quasienergy spectra change from completely real to complex, leading to the closing of the quasienergy gap. The nonanalyticities can then be understood on the same ground as those at topological phase boundaries in the unitary dynamics.

VI. FINAL REMARKS

By detecting winding numbers of three and four, our experiment establishes the feasibility of detecting higher winding numbers through loss in multistep QW dynamics. We show that as few as four (three) time steps are sufficient to detect winding numbers of three and four under appropriate parameters. Whereas the implementation and detection of FTPs of even larger winding numbers are possible in our experimental setup by improving the experimental apparatus (see the Appendixes), a promising setup with even better extendability are QWs in the time domain, where by translating the position of the walker into arrival times at the detector, the number of time steps can be significantly increased [51–53]. Such an extension would significantly enrich the experimentally

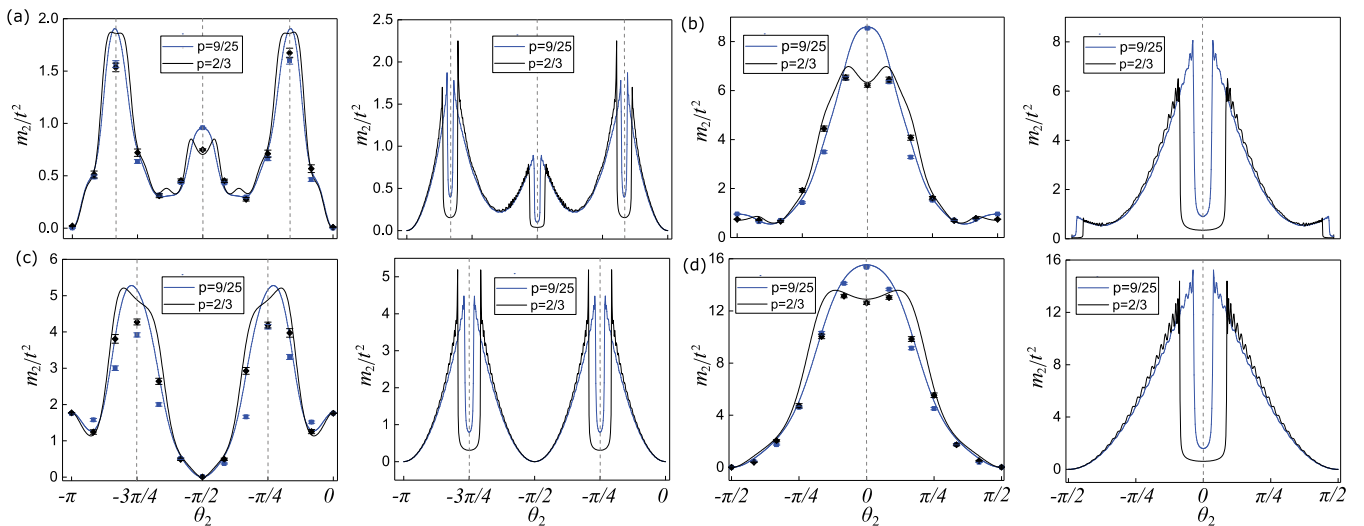


FIG. 5. Statistical moments m_2/t^2 of the walker position distribution for three-step nonunitary QWs governed by \tilde{U}'_3 (upper layer) and for four-step nonunitary QWs governed by \tilde{U}'_4 (lower layer), with the loss parameters $p = 9/25, 2/3$. (a),(c) Coin parameters (θ_1, θ_2) are scanned along the dotted lines in the phase diagrams of Figs. 2(a) and 4(a). (b),(d) Coin parameters are scanned along $\theta_1 = 0$. Experimental results of m_2/t^2 of up to four time steps (three time steps) and numerical simulations up to 50 time steps are shown in left and right columns, respectively. The vertical dashed lines indicate locations of topological phase transition from theoretical predictions.

accessible nonunitary FTPs in one dimension and would stimulate further studies on dynamic properties of nonunitary FTPs.

Another interesting direction would be the exploration of the relation between FTPs in nonunitary quantum-walk dynamics and those in a parity-time-symmetric configuration [12,50]. This is particularly relevant due to the existence of hidden pseudounitariness in our system, which is intimately connected with the reality of the quasienergy spectrum and hence with parity-time symmetry as well. Our experiment opens up the avenue toward a hierarchy of FTPs with large winding numbers and sheds light on understanding topological phenomena in nonunitary systems.

ACKNOWLEDGMENTS

This work has been supported by the Natural Science Foundation of China (Grants No. 11474049, No. 11674056, and No. 11522545) and the Natural Science Foundation of Jiangsu Province (Grant No. BK20160024). L.X. is supported by Postgraduate Research & Practice Innovation Program of Jiangsu Province. W.Y. acknowledges support from the National Key R&D Program (Grants No. 2016YFA0301700 and No. 2017YFA0304800). H.O. is supported by a Grant-in-Aid for Scientific Research on Innovative Areas ‘‘Topological Materials Science’’ (Grants No. JP16H00975 and No. JP15K21717) and JSPS KAKENHI (Grants No. JP16K17760 and No. JP16K05466). B.C.S. acknowledges financial support from the 1000-Talent Plan.

L.X. and X.Q. contributed equally to this work.

APPENDIX A: EXPERIMENTAL REALIZATION OF MULTISTEP NONUNITARY QUANTUM WALKS

At the start of a single-photon quantum walk (QW), a pair of photons is generated via type-I spontaneous parametric down conversion, with one photon serving as a trigger. The other photon is projected into the state $|+\rangle$ with a polarizing beam splitter (PBS) and a half-wave plate (HWP) heralded by the trigger photon, and is then sent to the quantum-walk interferometric setup. We implement the coin operator $R(\theta) = \mathbb{1}_w \otimes e^{-i\theta\sigma_y}$, the shift operator $S = \sum_x (|x-1\rangle\langle x| \otimes |H\rangle\langle H| + |x+1\rangle\langle x| \otimes |V\rangle\langle V|)$, and

the partial measurement operator M_e , following the approach outlined in [26]. Here, $\sigma_y = i(-|H\rangle\langle V| + |V\rangle\langle H|)$ is the standard Pauli operator under the polarization basis.

Losses are used to detect winding numbers in our experiment and can be controlled by the transmissivity of the partial polarizing beam splitter. Each pair of beam displacers forms an interferometer and their misalignment gives rise to pure dephasing, which is the major form of decoherence in the system. Furthermore, the surfaces of the beam displacers are not strictly smooth due to manufacturing inaccuracy. These should give rise to position-dependent dephasing throughout the QW. However, the dephasing caused by misalignment between beam displacers and imperfectness of the surface of the beam displacer can be compensated experimentally. Ideally, losses and misalignment of beam displacers do not limit the number of steps. The limitation on the number of steps depends on the size of the clear aperture of the beam displacer, which can be relaxed at the cost of beam displacers with larger clear apertures. Therefore, whereas we demonstrate that, by choosing the proper parameters, as few as four (three) steps are enough to have a clear detection of higher winding numbers, four (three) steps are not the limit of our experimental setups.

APPENDIX B: CHOICE OF TOPOLOGICAL FLOQUET OPERATORS

As we have discussed previously, \tilde{U}'_3 and \tilde{U}'_4 are topologically nontrivial so long as they possess chiral symmetry in the unitary limit. This allows us freedom in the design of multistep QWs. As an example, we consider four-step nonunitary QWs under the Floquet operators

$$\tilde{W}'_4 = MR\left(\frac{\theta_1}{2}\right)SR(\theta_2)SSR(\theta_2)SR\left(\frac{\theta_1}{2}\right), \quad (\text{B1})$$

$$\tilde{W}''_4 = MSR(\theta_2)SR\left(\frac{\theta_1}{2}\right)R\left(\frac{\theta_1}{2}\right)SR(\theta_2)S. \quad (\text{B2})$$

The corresponding phase diagram is shown in Fig. 6, which is richer than that of the four-step QW in the main text. We then calculated average displacements under \tilde{W}'_4 with different loss parameters; the results are shown in the middle and right panels of Fig. 6. Whereas under our parameters, the average

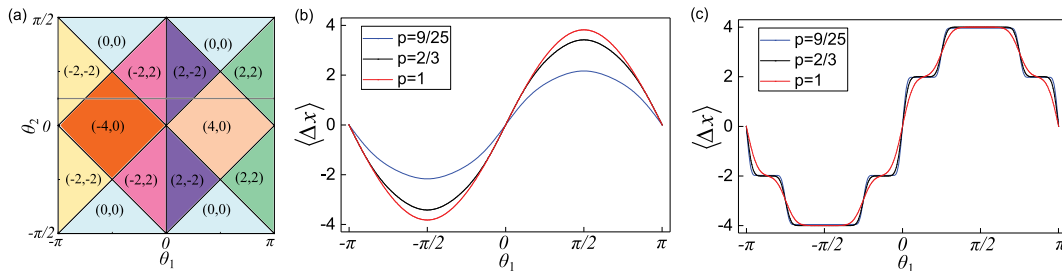


FIG. 6. Left: phase diagram for new four-step nonunitary QWs in terms of the topological invariants (v', v'') . (v', v'') are calculated from the Floquet operators \tilde{W}'_4 and \tilde{W}''_4 , respectively. Middle: average displacements under \tilde{W}'_4 for three time steps. Coin parameters vary along the gray line $\theta_2 = \pi/8$ in the phase diagram. The colored solid curve indicates numerical simulations for different loss parameters. The blue solid lines indicate $p = 9/25$, black solid lines indicate $p = 2/3$, and red solid lines indicate $p = 1$. The walker starts from $x = 0$ and the initial coin state was chosen as $|+\rangle$. Right: average displacements under \tilde{W}'_4 for 20 time steps. Other parameters are the same as those of the middle panel.

displacements have not yet converged at four time steps, the topological nature of \widetilde{W}'_4 is revealed by the quantized average displacements at long times.

APPENDIX C: STATISTICAL MOMENTS OF QUANTUM WALKS

In this section, we examine the statistical moments of both the unitary and the nonunitary QWs. Consider a general homogeneous QW driven by the Floquet operator $U = n_0\sigma_0 - i\mathbf{n} \cdot \sigma$. Assuming the walker starts from $x = 0$ at $t = 0$, we write the initial state of the walker-coin system as $|\Psi_0\rangle = |x = 0\rangle \otimes |\psi_0\rangle$, where $|\psi_0\rangle$ represents the coin state. At any given time step $t > 0$, we have $|\Psi_t\rangle = U^t|\Psi_0\rangle$, and the probability of measuring the walker at position x is

$$p(x, t) = \langle \Psi_t | x \rangle \langle x | \otimes \mathbb{1}_c | \Psi_t \rangle. \quad (\text{C1})$$

The j th statistical moment of this distribution is given by $m_j(t) = \langle x^j \rangle_t = \sum_x x^j p(x, t)$. In particular, we write the second moment in the momentum space as

$$m_2(t) = \int_{-\pi}^{\pi} \frac{dk}{2\pi} \langle \psi_0 | U^{\dagger t} \left(-i \frac{d}{dk} \right)^2 U^t | \psi_0 \rangle. \quad (\text{C2})$$

For the unitary QWs, we have $U = \cos E_k \sigma_0 - i \sin E_k (\hat{\mathbf{n}}_k \cdot \sigma)$ and hence $U^t = \cos(E_k t) \sigma_0 - i \sin(E_k t) (\hat{\mathbf{n}}_k \cdot \sigma)$, where $\hat{\mathbf{n}}_k = \mathbf{n}_k / \sin E_k$ and $\cos E_k = n_0$. It is then straightforward to derive

$$\begin{aligned} \frac{m_2(t)}{t^2} &= \int_{-\pi}^{\pi} \frac{dk}{2\pi} v_k^2 + O(1/t^2), \\ \int_{-\pi}^{\pi} \frac{dk}{2\pi} v_k^2 &= \int_{-\pi}^{\pi} \frac{dk}{2\pi} \left(\frac{dE_k}{dk} \right)^2 = \int_{-\pi}^{\pi} \frac{dk}{2\pi} \frac{1}{1 - n_0^2} \left(\frac{dn_0}{dk} \right)^2, \end{aligned} \quad (\text{C3})$$

where $v_k = \frac{dE_k}{dk}$ is the group velocity. At the topological phase boundary, the bulk gap closes at certain points in the momentum space, and the corresponding $n_0(k)$ at these momenta approaches zero. This gives rise to the slope discontinuity, as well as a peak structure of the second moment near the phase boundary [11].

For the nonunitary QWs in general, analytic expressions such as Eq. (C3) are typically unavailable. From numerical calculations (see Fig. 7), we see that signatures of topological phase transitions in the second moments persist in the nonunitary cases. In fact, at short time steps or away from the topological phase boundary, the second moments from the unitary and the nonunitary QWs are almost the same. However, at longer time steps, precipitous dips emerge in the second moment of nonunitary QWs near topological phase transitions. Such a behavior can be explained by mapping the Floquet operators in Eqs. (1), (3), and (4) to operators with the so-called pseudounitariness.

For such a purpose, we replace M with γM in Eqs. (1), (3), and (4) of the main text, and define $\overline{U}'_i := \gamma \widetilde{U}'_i$ and $\overline{U}''_i := \gamma \widetilde{U}''_i$, with $i = 3, 4$ and $\gamma = (1 - p)^{-\frac{1}{4}}$. Following the definition of winding numbers in the previous sections, it is straightforward to show that the topological phase diagrams for QWs are not changed with the introduction of γ in the Floquet operators. Further, as γ is a constant, it only

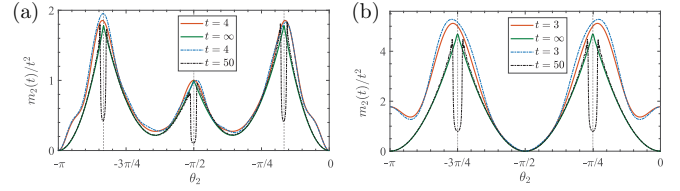


FIG. 7. Statistical moments $m_2(t)/t^2$ of the walker position distribution for unitary (solid curves) and nonunitary (dotted-dashed curves), three-step (upper layer), and four-step (lower layer) QWs, governed by $U'_3, \widetilde{U}'_3, U'_4,$ and \widetilde{U}'_4 , respectively. The green solid curves indicate the analytical results of the second moment [see Eq. (C3)], the vertical dashed lines indicate the locations of topological phase transitions from theoretical predictions, and the other curves indicate the numerical simulation results. The coin parameters are the same as those of Fig. 5 in the main text.

introduces a spatially homogeneous decay γ^t to the walker at the t th step, which does not change the statistical moments at any given time. Most importantly, as we will show in the next section, both \overline{U}'_i and \overline{U}''_i have pseudounitariness regions on the phase diagram, which depend on both the loss parameter p and the coin parameters.

In Figs. 8(a) and 8(b), we show the boundary between regions with pseudounitariness and those without using red lines. Typically, the pseudounitariness is lost in regions surrounding the topological phase boundaries. As pseudounitariness is a necessary and sufficient condition for the reality of the quasienergy spectrum of the effective non-Hermitian Hamiltonian, the loss of pseudounitariness leads to imaginary-valued quasienergies at certain points in momentum space. The resultant nonpseudounitary QW has similar behavior to a nonunitary QW with a broken parity-time symmetry, in that the long-time spatial distribution of the walker is Gaussian-like rather than ballistic [see Fig. 8(c)]. Hence the second moment decreases rapidly close to a topological phase transition, which carries over to the quantum-walk dynamics governed by the operators \widetilde{U}'_i and \widetilde{U}''_i , so long as the evolution time is long enough.

APPENDIX D: PSEUDOUNITARINESS

In this section, we define and discuss pseudounitariness. We show that pseudounitariness of a Floquet operator U is equivalent to the reality of the quasienergy spectrum of the corresponding effective Hamiltonian [46–48]. A necessary and sufficient condition for the spectrum of a non-Hermitian Hamiltonian to be purely real can be formulated in terms of pseudo-Hermiticity [47,48]. Such a condition can be generalized to the Floquet operator, where a Floquet operator U has η pseudounitariness [46] if it satisfies $U^{-1} = \eta U^\dagger \eta^{-1}$; here η is a Hermitian invertible linear operator.

In general, a nonunitary Floquet operator U has a complete set of biorthonormal eigenvectors $\{|\psi_\pm\rangle, |\chi_\pm\rangle\}$. Therefore, in momentum space,

$$\begin{aligned} U_k &= n_0\sigma_0 - in_1\sigma_x - in_2\sigma_y - in_3\sigma_z, \\ U_k^\dagger &= n_0\sigma_0 + in_1^*\sigma_x + in_2^*\sigma_y + in_3^*\sigma_z, \end{aligned}$$

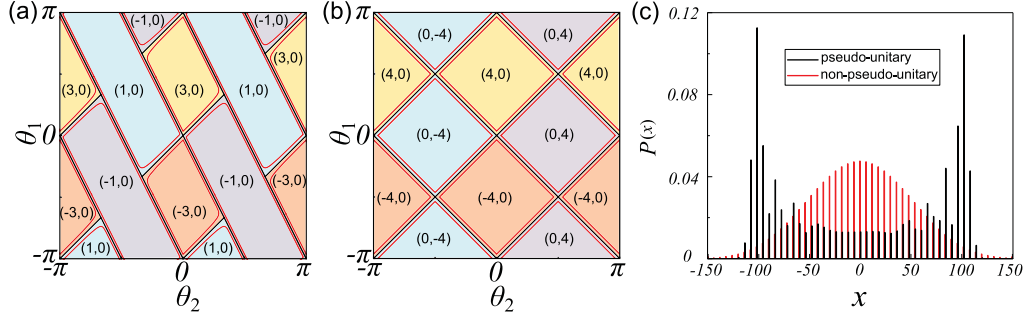


FIG. 8. Phase diagrams of three-step and (b) four-step Floquet operators \bar{U}'_i and \bar{U}''_i ($i = 3, 4$). Different topological phases are characterized by the winding numbers (v', v'') . The black lines mark the topological phase boundaries, which are the same as those of \tilde{U}'_i and \tilde{U}''_i . The red lines represent the boundaries between regions with pseudounitariness and those without. The pseudounitariness is lost in a loss-dependent region around the topological phase boundary. As the loss parameter p increases, the nonpseudounitary region also increases. (c) The long-time ($t = 50$) spatial distributions of the walker governed by the Floquet operator \bar{U}'_3 in the pseudounitary (black) and the nonpseudounitary (red) regions. The coin parameters are $(\theta_1 = \pi/4, \theta_2 = 0)$ and $(\theta_1 = 0, \theta_2 = 0)$, respectively, for the pseudounitary and the nonpseudounitary case. Note that the spatial distributions are the same as the normalized spatial distributions under \tilde{U}'_3 with the same coin parameters.

$$\begin{aligned}
 |\psi_{\pm}\rangle &= \frac{1}{\sqrt{2\sqrt{1-n_0^2}(\sqrt{1-n_0^2} \pm n_3)}} \\
 &\quad \times (n_3 \pm \sqrt{1-n_0^2}, n_1 + in_2)^T, \\
 \langle\chi_{\pm}| &= \frac{1}{\sqrt{2\sqrt{1-n_0^2}(\sqrt{1-n_0^2} \pm n_3)}} \\
 &\quad \times (n_3 \pm \sqrt{1-n_0^2}, n_1 - in_2), \\
 U_k|\psi_{\pm}\rangle &= \lambda_{\pm}|\psi_{\pm}\rangle, \quad U^{\dagger}|\chi_{\pm}\rangle = \lambda_{\pm}^*|\chi_{\pm}\rangle, \\
 \langle\chi_{\mu}|\psi_{\nu}\rangle &= \delta_{\mu\nu}, \quad \sum_{\mu} |\psi_{\mu}\rangle\langle\chi_{\mu}| = 1, \\
 U_k &= \sum_{\mu} \lambda_{\mu} |\psi_{\mu}\rangle\langle\chi_{\mu}|, \quad (D1)
 \end{aligned}$$

where $\lambda_{\pm} = n_0 \mp i\sqrt{1-n_0^2}$. Note the parameters λ_{\pm} , n_0 , n_1 , n_2 , and n_3 are all momentum dependent.

We define the effective Hamiltonian via $U_k = \exp(-iH_{\text{eff}})$. The quasienergy of H_{eff} is real if and only if $|\lambda_{\pm}| = 1$, which is the case when $n_0^2 \leq 1$. Let $\{|\phi_{\mu}\rangle\}$ be an arbitrary complete orthonormal basis, i.e., $\langle\phi_{\mu}|\phi_{\nu}\rangle = \delta_{\mu\nu}$, $\sum_{\mu=\pm} |\phi_{\mu}\rangle\langle\phi_{\mu}| = 1$ (for example $|\phi_{+}\rangle = |+\rangle$, $|\phi_{-}\rangle = |-\rangle$). We define $O := \sum_{\mu} |\psi_{\mu}\rangle\langle\phi_{\mu}|$ and $U_0 := \sum_{\mu} \lambda_{\mu} |\phi_{\mu}\rangle\langle\phi_{\mu}|$. It is straightforward to show that O is invertible with the inverse given by $O^{-1} = \sum_{\mu} |\phi_{\mu}\rangle\langle\chi_{\mu}|$ and $O^{-1}U_kO = U_0$. While $|\lambda_{\pm}| = 1$, U_0 is unitary with $U_0U_0^{\dagger} = 1$. Therefore, we have $O^{-1}U_kO(O^{-1}U_kO)^{\dagger} = 1$. Defining $\eta := OO^{\dagger}$, we have $U_k^{-1} = \eta U_k^{\dagger}(\eta)^{-1}$; i.e., U_k is η pseudounitary. Pseudounitariness of U_k is the direct result of the reality of the quasienergy at the momentum k .

Conversely, if U_k is η pseudounitary, we have $U_0U_0^{\dagger} = 1$, which leads to $|\lambda_{\pm}| = 1$ and the reality of the quasienergy of H_{eff} at the corresponding momentum k . Thus the reality of the quasienergy is equivalent to the pseudounitariness of the Floquet

operator U_k . It is also apparent that the pseudounitariness of U_k breaks down when $n_0^2 > 1$.

The Floquet operators \bar{U}'_i and \bar{U}''_i defined in the previous section possess pseudounitariness when their corresponding $n_0^2 \leq 1$ for all k . The boundaries between regions with pseudounitariness and those without are therefore calculated by requiring $n_0^2 = 1$ be satisfied for at least one k . We plot the boundary in Fig. 8 in red. It appears that, in both cases, the pseudounitariness is lost in the immediate vicinities of topological phase boundaries. We note that, as p increases, the widths of the nonpseudounitary regions also increase.

APPENDIX E: ROBUSTNESS AGAINST DISORDER

A key feature of topologically nontrivial systems is the robustness of topological properties against small perturbations. We find that the quantization of the average displacement of

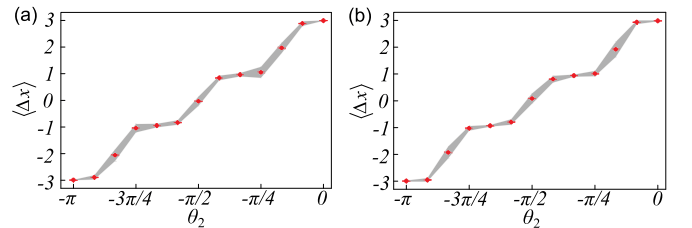


FIG. 9. Average displacements for three-step nonunitary QWs governed by \tilde{U}'_3 with either static disordered rotation angles (a) or dynamic disordered rotation angles (b). The loss parameter is fixed at $p = 1$. The disordered rotation angles are given by $\theta_{1,2} + \delta\theta$, where $\delta\theta$ is chosen from the interval $[-\pi/20, \pi/20]$. For static disorder, $\delta\theta$ is unique for each position and is independent of time. For dynamic disorder, $\delta\theta$ is unique for each time step and is independent of the position of the walker. The coin parameters (θ_1, θ_2) are scanned along the dotted line in the phase diagram [Fig. 2(a) in the main text]. The symbols and the gray shadings, respectively, indicate mean values of the measured average displacements and the range of the standard deviations averaged over 10 different ensembles for each pair of (θ_1, θ_2) . Experimental errors are due to photon-counting statistics.

the multistep nonunitary QW here is robust against both static and dynamic disorders. Our results therefore not only confirm the robustness of the measurement scheme, but also demonstrate the robustness of the FTPs with large topological invariants. Here, we use the three-step nonunitary QW for the evolution operator \tilde{U}'_3 with loss parameter $p = 1$ as an example.

First, to test the robustness of the quantization of the average displacement against static disorder, we keep the mean values of the coin parameters $\langle\theta_1\rangle$ and $\langle\theta_2\rangle$ on the line $\langle\theta_1\rangle = \langle\theta_2\rangle + \pi/2$ and measure the probabilities of the three-step nonunitary QW up to four time steps. We implement quantum-walk dynamics governed by the evolution operator \tilde{U}'_3 with 10 randomly generated coin rotations $R(\langle\theta_{1,2}\rangle + \delta\theta)$ for each position. For static disorder, the time-independent $\delta\theta$ is unique for each position and chosen from the intervals $[-\pi/20, \pi/20]$. In our experiment, $\delta\theta$ is implemented by

manipulating the setting angles of HWPs by small random amounts $\delta\theta$ around the coin parameters (θ_1, θ_2) . We then calculate the mean values of the 10 sets of average displacements. As shown in Fig. 9(a), the mean values of the average displacements are still quantized.

Second, we study the effect of the dynamic disorder. To generate dynamic disorder, a time-dependent coin rotation is required. The setting angles of HWPs for each step are modulated by a small random amount around the coin parameters (θ_1, θ_2) . The strength of the disorder is determined by the angle shift $\delta\theta$, which is randomly generated at each time step from the interval $[-\pi/20, \pi/20]$. Note that $\delta\theta$ here is time dependent but spatially homogeneous. We measure the probabilities and calculate the mean values of the 10 sets of average displacements. The results shown in Fig. 9(b) agree with theoretical predictions.

-
- [1] M. Z. Hasan and C. L. Kane, Colloquium: Topological insulators, *Rev. Mod. Phys.* **82**, 3045 (2010).
- [2] X. L. Qi and S. C. Zhang, Topological insulators and superconductors, *Rev. Mod. Phys.* **83**, 1057 (2011).
- [3] S. Ryu, A. P. Schnyder, A. Furusaki, and A. W. W. Ludwig, Topological insulators and superconductors: Tenfold way and dimensional hierarchy, *New J. Phys.* **12**, 065010 (2010).
- [4] J. C. Y. Teo and C. L. Kane, Topological defects and gapless modes in insulators and superconductors, *Phys. Rev. B* **82**, 115120 (2010).
- [5] Y. L. Chen, J. G. Analytis, J. H. Chu, Z. K. Liu, S. K. Mo, X. L. Qi, H. J. Zhang, D. H. Lu, X. Dai, Z. Fang, S. C. Zhang, I. R. Fisher, Z. Hussain, and Z. X. Shen, Experimental realization of a three-dimensional topological insulator, Bi_2Te_3 , *Science* **325**, 178 (2009).
- [6] Y. Xia, D. Qian, D. Hsieh, L. Wray, A. Pal, H. Lin, A. Bansil, D. H. Grauer, Y. S. Hor, R. J. Cava, and M. Z. Hasan, Observation of a large-gap topological-insulator class with a single Dirac cone on the surface, *Nat. Phys.* **5**, 398 (2009).
- [7] Z. Wang, Y. Chong, J. D. Joannopoulos, and M. Soljačić, Observation of unidirectional backscattering-immune topological electromagnetic states, *Nature (London)* **461**, 772 (2009).
- [8] L. Lu, J. D. Joannopoulos, and M. Soljačić, Topological photonics, *Nat. Photon.* **8**, 821 (2014).
- [9] T. Kitagawa, M. A. Broome, A. Fedrizzi, M. S. Rudner, E. Berg, I. Kassal, A. Aspuru-Guzik, E. Demler, and A. G. White, Observation of topologically protected bound states in photonic quantum walks, *Nat. Commun.* **3**, 882 (2012).
- [10] S. A. Skirlo, L. Lu, Y. Igarashi, Q. Yan, J. Joannopoulos, and M. Soljačić, Experimental Observation of Large Chern Numbers in Photonic Crystals, *Phys. Rev. Lett.* **115**, 253901 (2015).
- [11] F. Cardano, M. Maffei, F. Massa, B. Piccirillo, C. De Lisio, G. De Filippis, V. Cataudella, E. Santamato, and L. Marrucci, Statistical moments of quantum-walk dynamics reveal topological quantum transitions, *Nat. Commun.* **7**, 11439 (2016).
- [12] L. Xiao, X. Zhan, Z. H. Bian, K. K. Wang, X. Zhang, X. P. Wang, J. Li, K. Mochizuki, D. Kim, N. Kawakami, W. Yi, H. Obuse, B. C. Sanders, and P. Xue, Observation of topological edge states in parity-time-symmetric quantum walks, *Nat. Phys.* **13**, 1117 (2017).
- [13] C. Poli, M. Bellec, U. Kuhl, F. Mortessagne, and H. Schemm, Selective enhancement of topologically induced interface states in a dielectric resonator chain, *Nat. Commun.* **6**, 6710 (2015).
- [14] M. Bellec, U. Kuhl, G. Montambaux, and F. Mortessagne, Topological Transition of Dirac Points in a Microwave Experiment, *Phys. Rev. Lett.* **110**, 033902 (2013).
- [15] W. Hu, J. C. Pillay, K. Wu, M. Pasek, P. P. Shum, and Y. D. Chong, Measurement of a Topological Edge Invariant in a Microwave Network, *Phys. Rev. X* **5**, 011012 (2015).
- [16] R. Süssstrunk and S. D. Huber, Observation of phononic helical edge states in a mechanical topological insulator, *Science* **349**, 47 (2015).
- [17] R. Fleury, A. B. Khanikaev, and A. Alu, Floquet topological insulators for sound, *Nat. Commun.* **7**, 11744 (2016).
- [18] G. Jotzu, M. Messer, R. Desbuquois, M. Lebrat, T. Uehlinger, D. Greif, and T. Esslinger, Experimental realization of the topological Haldane model with ultracold fermions, *Nature (London)* **515**, 237 (2014).
- [19] M. Leder, C. Grossert, L. Sitta, M. Genske, A. Rosch, and M. Weitz, Real-space imaging of a topologically protected edge state with ultracold atoms in an amplitude-chirped optical lattice, *Nat. Commun.* **7**, 13112 (2016).
- [20] E. J. Meier, F. A. An, and B. Gadway, Observation of the topological soliton state in the Su-Schrieffer-Heeger model, *Nat. Commun.* **7**, 13986 (2016).
- [21] M. Atala, M. Aidelsburger, J. T. Barreiro, D. Abanin, T. Kitagawa, E. Demler, and I. Bloch, Direct measurement of the Zak phase in topological Bloch bands, *Nat. Phys.* **9**, 795 (2013).
- [22] M. Aidelsburger, M. Lohse, C. Schweizer, M. Atala, J. T. Barreiro, S. Nascimbene, N. R. Cooper, I. Bloch, and N. Goldman, Measuring the Chern number of Hofstadter bands with ultracold bosonic atoms, *Nat. Phys.* **11**, 162 (2015).
- [23] N. Fläschner, B. S. Rem, M. Tarnowski, D. Vogel, D. S. Lühmann, K. Sengstock, and C. Weitenberg, Experimental reconstruction of the Berry curvature in a Floquet Bloch band, *Science* **352**, 1091 (2016).
- [24] V. V. Ramasesh, E. Flurin, M. Rudner, I. Siddiqi, and N. Y. Yao, Direct Probe of Topological Invariants using Bloch Oscillating Quantum Walks, *Phys. Rev. Lett.* **118**, 130501 (2017).

- [25] E. Flurin, V. V. Ramasesh, S. Hacothen-Gourgy, L. S. Martin, N. Y. Yao, and I. Siddiqi, Observing Topological Invariants using Quantum Walks in Superconducting Circuits, *Phys. Rev. X* **7**, 031023 (2017).
- [26] X. Zhan, L. Xiao, Z. H. Bian, K. K. Wang, X. Z. Qiu, B. C. Sanders, W. Yi, and P. Xue, Detecting Topological Invariants in Nonunitary Discrete-Time Quantum Walks, *Phys. Rev. Lett.* **119**, 130501 (2017).
- [27] X. P. Wang, L. Xiao, X. Z. Qiu, K. K. Wang, W. Yi, and P. Xue, Detecting topological invariants and revealing topological phase transitions in discrete-time photonic quantum walks, *Phys. Rev. A* **98**, 013835 (2018).
- [28] F. Cardano, A. D'Errico, A. Dauphin, M. Maffei, B. Piccirillo, C. De Lisio, G. De Filippis, V. Cataudella, E. Santamato, L. Marrucci, M. Lewenstein, and P. Massignan, Detection of Zak phases and topological invariants in a chiral quantum walk of twisted photons, *Nat. Commun.* **8**, 15516 (2017).
- [29] S. Barkhofen, T. Nitsche, F. Elster, L. Lorz, A. Gabris, I. Jex, and C. Silberhorn, Measuring topological invariants and protected bound states in disordered discrete time quantum walks, *Phys. Rev. A* **96**, 033846 (2017).
- [30] J. M. Zeuner, M. C. Rechtsman, Y. Plotnik, Y. Lumer, S. Nolte, M. S. Rudner, M. Segev, and A. Szameit, Observation of a Topological Transition in the Bulk of a Non-Hermitian System, *Phys. Rev. Lett.* **115**, 040402 (2015).
- [31] S. Mittal, S. Ganeshan, J. Fan, A. Vaezi, and M. Hafezi, Measurement of topological invariants in a 2D photonic system, *Nat. Photon.* **10**, 180 (2016).
- [32] M. S. Rudner, M. Levin, and L. S. Levitov, Survival, decay, and topological protection in non-Hermitian quantum transport, [arXiv:1605.07652](https://arxiv.org/abs/1605.07652).
- [33] J. K. Asbóth and H. Obuse, Bulk-boundary correspondence for chiral symmetric quantum walks, *Phys. Rev. B* **88**, 121406 (2013).
- [34] D. Kim, M. Ken, N. Kawakami, and H. Obuse, Floquet topological phases driven by \mathcal{PT} symmetric nonunitary time evolution, [arXiv:1609.09650](https://arxiv.org/abs/1609.09650).
- [35] M. S. Rudner and L. S. Levitov, Topological Transition in a Non-Hermitian Quantum Walk, *Phys. Rev. Lett.* **102**, 065703 (2009).
- [36] T. Rakovszky, J. K. Asbóth, and A. Alberti, Detecting topological invariants in chiral symmetric insulators via losses, *Phys. Rev. B* **95**, 201407 (2017).
- [37] T. Kitagawa, M. S. Rudner, E. Berg, and E. Demler, Exploring topological phases with quantum walks, *Phys. Rev. A* **82**, 033429 (2010).
- [38] P. Xue, H. Qin, B. Tang, and B. C. Sanders, Observation of quasiperiodic dynamics in a one-dimensional quantum walk of single photons in space, *New J. Phys.* **16**, 053009 (2014).
- [39] P. Xue, H. Qin, and B. Tang, Trapping photons on the line: Controllable dynamics of a quantum walk, *Sci. Rep.* **4**, 04825 (2014).
- [40] P. Xue, R. Zhang, H. Qin, X. Zhan, Z. H. Bian, J. Li, and B. C. Sanders, Experimental Quantum-Walk Revival with a Time-Dependent Coin, *Phys. Rev. Lett.* **114**, 140502 (2015).
- [41] Z. H. Bian, J. Li, H. Qin, X. Zhan, R. Zhang, B. C. Sanders, and P. Xue, Realization of Single-Qubit Positive-Operator-Valued Measurement via a One-Dimensional Photonic Quantum Walk, *Phys. Rev. Lett.* **114**, 203602 (2015).
- [42] P. Xue, R. Zhang, Z. H. Bian, X. Zhan, H. Qin, and B. C. Sanders, Localized state in a two-dimensional quantum walk on a disordered lattice, *Phys. Rev. A* **92**, 042316 (2015).
- [43] J. A. Izaac, X. Zhan, Z. H. Bian, K. K. Wang, J. Li, J. B. Wang, and P. Xue, Centrality measure based on continuous-time quantum walks and experimental realization, *Phys. Rev. A* **95**, 032318 (2017).
- [44] Z. H. Bian, J. Li, X. Zhan, J. Twamley, and P. Xue, Experimental implementation of a quantum walk on a circle with single photons, *Phys. Rev. A* **95**, 052338 (2017).
- [45] P. Xue, X. Zhang, K. K. Wang, X. Zhan, and X. P. Wang, Implementing arbitrary coined two-dimensional quantum walks via bulk optical interferometry, *Opt. Commun.* **426**, 558 (2018).
- [46] A. Mostafazadeh, Pseudounitary operators and pseudounitary quantum dynamics, *J. Math. Phys.* **45**, 932 (2004).
- [47] A. Mostafazadeh, Pseudo-Hermiticity versus \mathcal{PT} symmetry: The necessary condition for the reality of the spectrum of a non-Hermitian Hamiltonian, *J. Math. Phys.* **43**, 205 (2002).
- [48] A. Mostafazadeh, Pseudo-Hermiticity versus \mathcal{PT} -symmetry. II. A complete characterization of non-Hermitian Hamiltonians with a real spectrum, *J. Math. Phys.* **43**, 2814 (2002).
- [49] A. Regensburger, C. Bersch, M. A. Miri, G. Onishchukov, D. N. Christodoulides, and U. Peschel, Parity-time synthetic photonic lattices, *Nature (London)* **488**, 167 (2012).
- [50] K. Mochizuki, D. Kim, and H. Obuse, Explicit definition of \mathcal{PT} symmetry for nonunitary quantum walks with gain and loss, *Phys. Rev. A* **93**, 062116 (2016).
- [51] A. Schreiber, K. N. Cassemiro, V. Potoček, A. Gábris, P. J. Mosley, E. Andersson, I. Jex, and C. Silberhorn, Photons Walking the Line: A Quantum Walk with Adjustable Coin Operations, *Phys. Rev. Lett.* **104**, 050502 (2010).
- [52] A. Schreiber, K. N. Cassemiro, V. Potoček, A. Gábris, I. Jex, and C. Silberhorn, Decoherence and Disorder in Quantum Walks: From Ballistic Spread to Localization, *Phys. Rev. Lett.* **106**, 180403 (2011).
- [53] A. Schreiber, A. Gábris, P. P. Rohde, K. Laiho, M. Štefaňák, V. Potoček, C. Hamilton, I. Jex, and C. Silberhorn, A 2D quantum walk simulation of two-particle dynamics, *Science* **336**, 55 (2012).